







Article

A Novel Emergency Gas-to-Power System Based on an Efficient and Long-Lasting Solid-State Hydride Storage System: Modeling and Experimental Validation

David Michael Dreistadt ^{1,*}, Julián Puszkiel ^{1,2}, José Maria Bellosta von Colbe ¹, Giovanni Capurso ¹, Gerd Steinebach ³, Stefanie Meilinger ³, Thi-Thu Le ¹, Myriam Covarrubias Guarneros ², Thomas Klassen ^{1,2} and Julian Jepsen ^{1,2}

¹ Helmholtz-Zentrum hereon GmbH, Institute of Hydrogen Technology, Max-Planck-Straße 1, 21502 Geesthacht, Germany; julian.puszkiel@hereon.de (J.P.); jose.bellostavoncolbe@hereon.de (J.M.B.v.C.); giovanni.capurso@hereon.de (G.C.); thi.le@hereon.de (T.-T.L.); thomas.klassen@hereon.de (T.K.); julian.jepsen@hereon.de (J.J.)

² Institute of Material Science, Helmut Schmidt University, Holstenhofweg 85, 22043 Hamburg, Germany; myriam.covarrubias@hereon.de

³ Hochschule Bonn-Rhein-Sieg, Institut für Technik Ressourcenschonung und Energieeffizienz, Grantham-Allee 20, 53757 Sankt Augustin, Germany; gerd.steinebach@h-brs.de (G.S.); stefanie.meilinger@h-brs.de (S.M.)

* Correspondence: david.dreistadt@hereon.de; Tel.: +49-4152-87-2565



Citation: Dreistadt, D.M.; Puszkiel, J.; Bellosta von Colbe, J.M.; Capurso, G.; Steinebach, G.; Meilinger, S.; Le, T.-T.; Covarrubias Guarneros, M.; Klassen, T.; Jepsen, J. A Novel Emergency Gas-to-Power System Based on an Efficient and Long-Lasting Solid-State Hydride Storage System: Modeling and Experimental Validation. *Energies* **2022**, *15*, 844. <https://doi.org/10.3390/en15030844>

Academic Editor: Mofazzal Hossain

Received: 7 December 2021

Accepted: 20 January 2022

Published: 24 January 2022

Publisher's Note: MDPI stays neutral with regard to jurisdictional claims in published maps and institutional affiliations.



Copyright: © 2022 by the authors. Licensee MDPI, Basel, Switzerland. This article is an open access article distributed under the terms and conditions of the Creative Commons Attribution (CC BY) license (<https://creativecommons.org/licenses/by/4.0/>).

Abstract: In this paper, a gas-to-power (GtoP) system for power outages is digitally modeled and experimentally developed. The design includes a solid-state hydrogen storage system composed of TiFeMn as a hydride forming alloy (6.7 kg of alloy in five tanks) and an air-cooled fuel cell (maximum power: 1.6 kW). The hydrogen storage system is charged under room temperature and 40 bar of hydrogen pressure, reaching about 110 g of hydrogen capacity. In an emergency use case of the system, hydrogen is supplied to the fuel cell, and the waste heat coming from the exhaust air of the fuel cell is used for the endothermic dehydrogenation reaction of the metal hydride. This GtoP system demonstrates fast, stable, and reliable responses, providing from 149 W to 596 W under different constant as well as dynamic conditions. A comprehensive and novel simulation approach based on a network model is also applied. The developed model is validated under static and dynamic power load scenarios, demonstrating excellent agreement with the experimental results.

Keywords: gas-to-power; hydrides; hydrogen storage; fuel cell; modeling; hydrogen

1. Introduction

In today's society, fossil fuels are increasingly becoming a problem due to their significant environmental impact; the call for alternative energy sources is becoming louder [1–3]. The utilization of renewable energy sources is finding more and more acceptance in society and plays a crucial role in the political and economic situation [4]. In the last 20 years, much effort has been put into developing systems to integrate renewable sources into the current energy system [5]. Gielen et al. [6] reported on the acceleration of the energy transition, which would enable two-thirds of the world's energy demand to be supplied by renewable energy sources by 2050. This accelerated transition towards renewable sources would limit the global temperature increase to below 2 °C.

The use of renewable energy sources, especially energy storage, has become the focus of intensive research since energy production is strongly influenced by environmental factors (e.g., weather) [5]. Hydrogen, which can be produced from a variety of renewable energy sources, offers an efficient and clean alternative to fossil fuels. It has a weight-related energy content of 33.3 kWh/kg, significantly higher than gasoline with 8.5 kWh/kg. However, its volume-related energy content is significantly lower due to its low density with 0.003 kWh/L at 273.15 K and 1 bar. The use of hydrogen technology in the industry

and the energy sector offers several opportunities and presents a significant challenge. Some works [5,7,8] present complete overviews about the implemented hydrogen-based energy systems for mobile and stationary applications. As reported, there are several challenges to hydrogen as an energy carrier, with cost, efficiency, and durability emerging as the most critical.

For hydrogen as an energy carrier, its storage technology is a decisive factor. In addition to pressurized and liquefied gas storage systems, metal hydride-based storage systems (MH-systems) are suitable, especially for long-term storage. MH-systems are characterized mainly by high operational reliability and high volumetric storage density [9,10]. An important field of application intended for MH-systems are stationary power-to-gas (PtoG) and gas-to-power (GtoP) systems [5]. These integrated systems offer the advantage of producing green hydrogen through electrolysis from renewable electricity and re-converting stored hydrogen into electric power in a fuel cell when needed. The design and integration of MH-systems represent a challenge in terms of thermal management. The hydrogenation and dehydrogenation reactions of a hydride-forming alloy are exothermic and endothermic, respectively. Hence, heat must be removed for an effective absorption process and provided during the desorption process. A fundamental design parameter is thus effective thermal management to integrate the MH-systems into a GtoP and PtoG system. The design and control of the thermal management of such a system leads to an increase in overall efficiency. Hence, it allows operations to be as energy-saving and cost-effective as possible. A practical approach consists of utilizing waste heat from the fuel cell to supply heat to MH-tanks. Moreover, it is also possible to store the exothermal reaction heat resulting from the formation of metal hydride compounds in the MH-tanks, to be recycled when needed. As already reported in the literature, most of the experimental integrated systems (renewable energy source + electrolyzer + storage system + fuel cell) present relatively low efficiency and high costs [5]. Therefore, improving the overall efficiency of these integrated systems is demanding. A particularly interesting field of application is long-term energy storage, which is possible almost loss-free with MH-systems in contrast to battery systems. Thus, MH-systems offer excellent application possibilities for emergency power supply and represent a good alternative (e.g., for environmentally harmful diesel generators).

Optimizing the overall efficiency of such a system requires the development of models able to simulate the planned experimental set-up effectively. This approach reduces costs and time in building expensive experimental set-ups. In general, models involving 2D or 3D geometries are developed to design and/or investigate the MH-reservoir and not the system as a whole. Moreover, models in 3D geometries usually involve very high computational efforts and result in an unsuitable approach for system simulations [11–19]. Therefore, system simulations in 0D or 1D geometries are a fast and computationally efficient way to investigate how to improve efficiencies and reach cost-effective integrated systems. In this process, all relevant system components are described in terms of main physical properties by mathematical equations and implemented in a corresponding simulation environment.

System simulation approaches have been applied to different integrated configurations of PtoG/GtoP systems [20–24]. For example, system simulations of a MH-system based on a neuronal network for the PtoG/GtoP concept were already demonstrated [20]. It was found that the application of such an approach is necessary due to the high degree of non-linearity and a large number of unknown parameters. Other general simulation approaches were applied to represent gas or liquid fluid networks [21–23]. These simulation approaches for creating a network were based on coupling constraints for network nodes, defining how information propagates. The network makes it possible to also build up more complex systems, as demonstrated in [22,23]. However, due to the high degree of abstraction of the component models, it is usually necessary to calibrate system parameters carefully [23].

Another challenge with existing approaches for network simulation of GtoP/PtoG systems with integrated metal hydride storage is the predefined information to set the flow direction. These flow directions define the stream of the information (e.g., a mass flow)

for the entire system model. This method can lead to difficulties in complex networks, especially if it is unknown where the information should flow. An example of this flow approach can be found in [21], where system boundary conditions for an MH-tank define how much hydrogen flows into or out of the tank for hydrogenation and dehydrogenation processes, respectively. Thus, it is imperative to define appropriate boundary or coupling conditions for such models.

For the reasons mentioned above, further developing 1D or 0D system models is necessary to design and improve integrated systems composed of an MH, electrolyzer, and fuel cell. It must be taken into account, though, that geometry and other relevant properties are strongly abstracted, and hence a compromise between the degree of abstraction and computational efficiency must be reached.

This paper investigates the application of low-temperature metal hydride (TiFeMn) to GtoP systems for stationary emergency power supply. The herein-developed GtoP system (“MH2-Powerbank”) consists of five TiFeMn powder-filled MH-tanks, with a total weight of 6.7 kg, to supply hydrogen to an air-cooled 1.6 kW fuel cell. This GtoP system is experimentally tested and optimized by applying a novel network simulation approach. A network simulation model for the integrated fuel cell and MH-tank was built up. This approach includes the 0D MH-tank model. The simulation model was implemented in the MATLAB/Simscape environment and is based on conservation equations. The simulation model was also calibrated and validated with experimental results. Based on the system simulation, the overall GtoP system efficiency is optimized by investigating the most suitable parameters to utilize the waste heat of the air-cooled fuel cell as the heat supply for the desorption process of the hydride tanks.

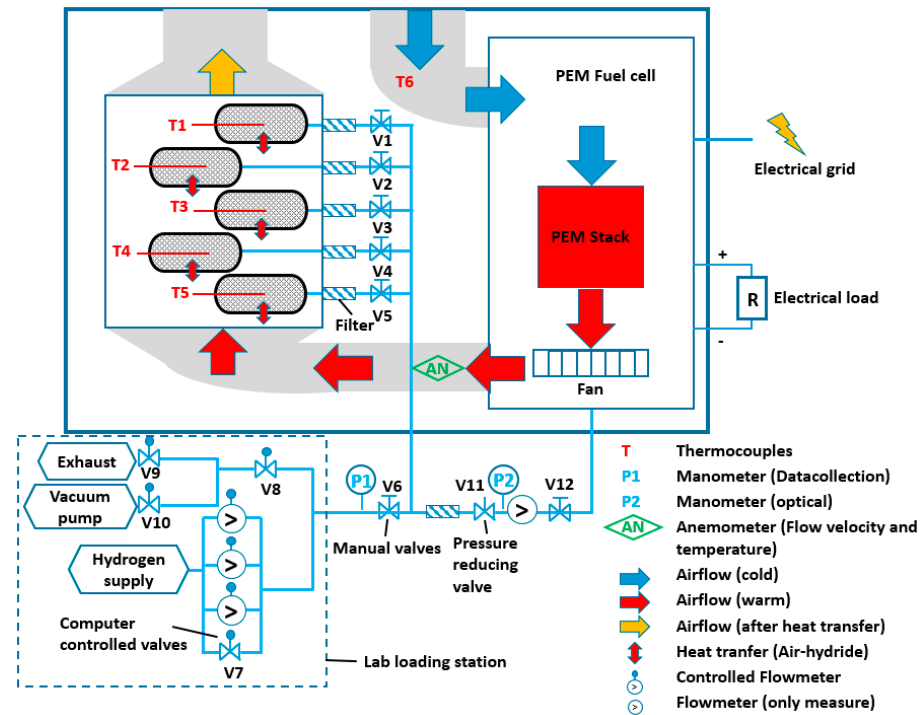
2. The Experimental Setup

2.1. Description of the Experimental Setup

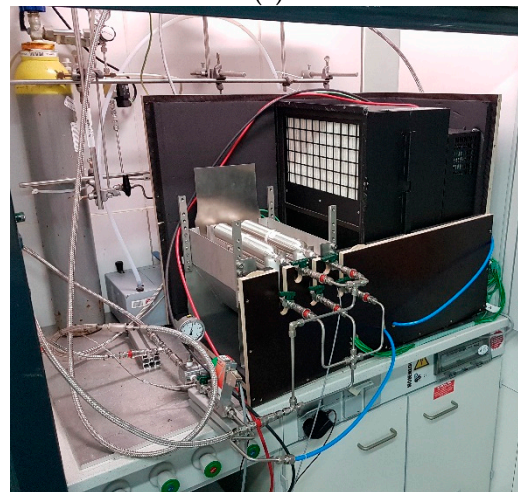
Figure 1 displays the basic design of the MH2-Powerbank test stand: a detailed sketch of the system (Figure 1a) and a photograph of the experimental set-up (Figure 1b). The set-up was originally designed to connect the fuel cell with the direct hydrogen supply from an already existing loading station in the laboratory, as illustrated in Figure 1. The fuel cell was cooled with forced convection using a fan that provided airflow at room temperature (Figure 1a). The heated air entered an air duct and reached the hydride storage tanks (“red arrows”). In this way, the hydride storage tanks were heated with air to carry out the endothermic hydrogen desorption. In order to reduce the thermal losses, the whole system was placed in a closed and isolated cabinet. Several sensors were integrated into the illustrated experimental set-up to gather data to evaluate the system’s performance and use the data for the system simulation. The temperatures of the MH-tanks (T1–5), the inlet temperature (T6) of the cooling air stream, and the air stream’s outlet temperature after warming up (AN) were measured. The hydrogen pressure and hydrogen flow from the MH-tanks to the fuel cell were measured by a pressure transducer (P2) and a flowmeter (between the valves V11 and V12), respectively. The air speed from the fuel cell stack to the MH-tank was measured by an anemometer (AN).

An amount of 6.7 kg of TiFeMn powder with a theoretical maximum capacity of 1.73 wt.% [25], produced by GKN Powder Metallurgy GmbH and developed within the HyCare project (Hydrogen Carrier for Renewable Energy Storage), was used [25,26]. The TiFeMn powder was distributed in five tanks (each tank of 500 cm³ made of 316 L Stainless Steel, from the company Swagelok, Soren, OH, USA), as illustrated in Figure 1a. This low-temperature hydride was able to operate at pressures below 50 bar and loaded hydrogen at room temperatures. The 1.6 kW PEM (proton exchange membrane) Fuel Cell was from the type “DBX2000 power backup module”, produced by Dantherm Power (Figure 1a). It delivered a maximum power of 1.6 kW and needed a hydrogen supply of Grade 3.0 (99.9%) or higher. The system was made to provide constant power during power outages (i.e., in emergency cases). For this purpose, the PEM stack had an integrated electrical system. Such an integrated electrical system in a scale-up size can be connected to the public grid.

The PEM stacks also included an ultracapacitor for the initial provision of energy. Type K thermocouples from Thermocoax are able to measure in a range between $-200\text{ }^{\circ}\text{C}$ and $800\text{ }^{\circ}\text{C}$ were used. These kinds of thermocouples were utilized to measure the temperature in every tank and the system.



(a)



(b)

Figure 1. (a) Detailed sketch and (b) photo of the MH2-Powerbank.

The unit housing was made of wood and lined on the insides with insulating material (Figure 1b) to avoid heat conduction losses in the PEM stack. The air duct from the fuel cell to the MH-tanks was built of industrial metallic sheets made of steel (DIN/EN: X6CrNiMoTi17-12-2). Through these ducts, the exhaust air from the fuel cell was supplied to the hydrogen storage tanks.

The anemometer type SS 20.260 (Figure 1a, AN) from the company Schmidt Technology was used to measure the exhaust air velocity up to an air speed of 60 m/s , and the exhaust air temperature of the fuel cell (range between $-20\text{ }^{\circ}\text{C}$ and $120\text{ }^{\circ}\text{C}$).

The piping, valves, and all other gas piping components were made of stainless steel and purchased from the company Swagelok company. The piping was 6 mm in outer diameter. The hydrogen pressure to provide to the fuel cell was reduced to 1.4 bar with a manual pressure regulator (V11), with a range of outlet pressure between 0 and 3.4 bar. The fuel cell consumption was registered with a digital thermal mass flow meter for gases from the company Bronkhorst, with a measuring range for hydrogen between 0.084 to 13.6 NL/min (Figure 1a, between the valves V11 and V12).

Hydrogen gas (Linde; purity: 99.9999%) was supplied to load the station, which was already integrated into the laboratory and connected to the hydride tanks (Figure 1a: lab loading station). The desired hydrogen amount was provided to the tanks' system via mass flow controllers from the company Bronkhorst. The inflow volume was controlled in a range from 0 to 250 NL/min. For all data recording and control, a program was created in LabVIEW (National Instruments, Austin, TX, USA).

2.2. Operating Scenarios and Test Parameters: MH2-Powerbank System

In this section, the operating scenarios and experimental parameters for the test of the system are described. Three different operating scenarios were designed to operate the system. The main test parameters, such as the resistance of the electronic load, duration of the experiment, and system power, were considered to evaluate the system performance.

2.2.1. Operating Scenarios

Scenario A. Loading of MH-tanks: In this operating scenario, the already activated hydride tanks were filled with hydrogen at room temperature through a controlled volumetric flow, coming from the loading station. Valves V7 to V12 were closed, and V1 to V6 were opened (Figure 1a). A PID-controller regulated the loading process of the tank, and it was performed until reaching the target pressure of 40 bar under a filling flowrate limited to 250 L/min. The complete loading of the tanks led to a total amount of stored hydrogen in the solid phase of about 105.5 g (i.e., 1.54 wt.% H₂ based on the Supplementary Material) (ESI, Figure S1). Moreover, the mass of hydrogen in the gas phase under 40 bar and 25 °C was about 5.3 g. Thus, the total amount of hydrogen in the loaded system was 110.8 g.

Scenario B. Coupling the loading station with the fuel cell: The fuel cell was tested to characterize its polarization curve (voltage vs. current) in this scenario. These tests were performed by supplying hydrogen to the fuel cell from the laboratory loading station (Figure 1a). The valves V1 to V5, V8 to V10, and the flowmeters were closed. The hydrogen pressure after the manual regulation valve V11 was set to 1.4 bar. However, the upstream system pressure during the experiments was variable between 5 bar and 8 bar.

Scenario C. Coupling between the MH-tanks and the fuel cell: This scenario aimed to evaluate the performance of the coupled system in power outages. The stored hydrogen in the MH-tanks was used to supply the fuel cell stack, mimicking a real scenario for which the system was designed. In this case, the MH-tanks were previously charged, as described in scenario A. In this mode, the line to connect the system with the loading station is closed (i.e., closed valves V7 to 10 and flowmeters). The valve V6 was opened to measure and register the pressure in P1 (Figure 1a). The hydrogen pressure was regulated by the manual valve V11 to 1.4 bar, which is the ideal inlet pressure of the fuel cell. At the beginning of this operating scenario, the integrated ultracapacitor supplied the needed energy, until the fuel cell started to operate.

2.2.2. Experimental Parameters

Table 1 displays the main experimental parameters used for the test performed with the MH2-Powerbank system. For such experiments, scenario C was applied. Tests 1 to 4 were carried out under constant resistances of the fuel cell from 5.0 Ohm to 20.0 Ohm. The consumed power under such resistance conditions ranged between 120 W and 478 W. This selected power range was determined based on the available amount of hydrogen in the MH-tanks. The experimental measurements, in the range of consumed power mentioned

above, were compared with the results of the developed system model and used for model validation. It was also possible to test higher power loads, up to a maximum of 1560 W to investigate the performance limits of the MH2-Powerbank (Not included in Table 1). However, due to the enormous hydrogen consumption of the fuel cell, the temperature of the MH-tanks drops too much. Hence, the MH-tanks could not provide the needed hydrogen to the fuel cell (thus, the figures relative to this load are not provided). In addition, tests 5 and 6 were performed to check the dynamic behavior under strongly varying power loads and representative of the daily profiles, respectively. More specifically, for test 5, the fuel cell power consumption started at 149 W for 15 min and then increased to 596 W for 5 min. Subsequently, the load was interchangeably set to 149 W for 15 min and 596 W for 5 min. Scenario 5 is also considered a high power load scenario. In the case of the daily profiles, test 6, a representative household with an annual power consumption of 1000 kWh/year, was applied [27]. For example, the quarter-hourly power values on a representative Saturday afternoon in winter from 5:00 p.m. were selected as time series data.

Table 1. Experimental parameters for the test performed with the MH2-Powerbank system, using scenario C.

Experiment	Resistance [Ohm]	Duration [h]	Power [W]
1	5.0	1.13	478
2	7.5	1.91	319
3	10.0	3.55	241
4	20.0	6.5	120
5	Large variations of power consumption	2.01	149–596
6	Representative of the daily profile	3.88	152–213

3. Mathematical Model

The system simulation model was developed in the environment MATLAB/Simulink. Utilizing the MATLAB/Simulink included the additional component library Simscape, which contained several mathematical component models [28]. This approach allowed the coupled simulation to form a network.

As illustrated in Figure 2, the MH-tanks are modeled in 0D geometry and the conceptual flow of information in terms of mass (\dot{m}_{H_2}) and heat (\dot{Q}_{WT}) is represented. The gas network refers to a hydrogen volume connected to the hydride tanks, and the heat exchange refers to the connection between the hydride tanks and an external heat exchanger through a fluid. The overall network model implemented in MATLAB/Simulink is provided in figure (Section 3.1.4).

Information flow principle

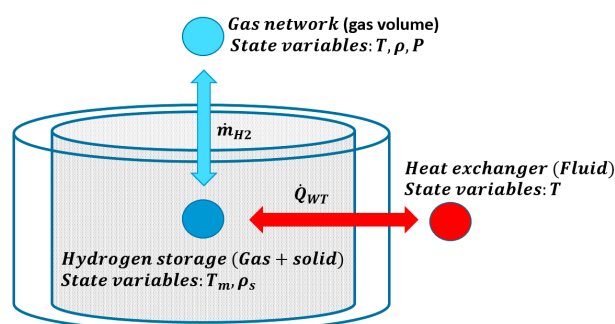


Figure 2. 0D model of the MH-tanks and conceptual mass and heat flow connections.

3.1. MH-Tanks and the Connections with the Network: Description of the 0D Model

The modeling of the hydride tanks was implemented in a 0D geometry by using MATLAB/Simulink. The TiFeMn alloy and its corresponding hydride are in powder form. For the development of the model, the following assumptions were made:

1. The hydrogen transport inside the porous medium's free volume is neglected due to the fast hydrogen velocity.
2. The local thermal equilibrium is assumed: temperatures in both fluid (hydrogen) and solid phases (alloy-hydride) are equal.
3. Hydrogen is considered an ideal gas due to the low working pressures.
4. The mass exchange caused by the chemical reaction occurs directly between the hydride-forming alloy and the connected gas network.
5. The heat exchange between the gas network and the hydride material is neglected.
6. The gas pressure in the porous bed (alloy-hydride) is assumed to be equal to that of the connected gas network. Therefore, the mass flow of hydrogen during the reaction occurs as part of the gas network.
7. The temperature change of the gas phase due to gas transport between the gas phase and the solid hydride is neglected.

The conservation equations used in the simulation model for the hydride formation are based on the ones reported in [23]. The change of mass of the solid phase (alloy-hydride phases) was calculated by applying the mass conservation law, according to Equation (1):

$$\epsilon \frac{d\rho_s}{dt} = \dot{m}_{rate}, \quad (1)$$

where $\rho_s \left[\frac{\text{kg}}{\text{m}^3} \right]$ is the density of the solid, $\epsilon [-]$ is the porosity of the powder bed, and $\dot{m}_{rate} \left[\frac{\text{kg}}{\text{m}^3 \text{ s}} \right]$ is the reaction rate per unit volume.

In order to calculate the energy change and thus the associated temperature change of the solid phase (hydride and gas phase together), the conservation of energy is applied, as illustrated in Equations (2) and (3):

$$\frac{d((\rho_m c_p)_e T_m)}{dt} = \dot{Q}_{HE} + \frac{\dot{m}_{rate}}{M_{H_2}} \cdot \Delta H, \quad (2)$$

with

$$(\rho_m c_p)_e = (\epsilon \rho_g c_{p,g} + (1 - \epsilon) \rho_s c_{p,s}), \quad (3)$$

where $\rho_g \left[\frac{\text{kg}}{\text{m}^3} \right]$ is the density of the gas, $T_m [\text{K}]$ is the equilibrium temperature of the gas and solid phases, as expressed in assumption 2, $c_{p,g} \left[\frac{\text{J}}{\text{kgK}} \right]$ or $c_{p,s} \left[\frac{\text{J}}{\text{kgK}} \right]$ is the specific heat capacity of gas or solid, $\dot{Q}_{HE} \left[\frac{\text{J}}{\text{m}^3 \text{ s}} \right]$ is the volume-based heat flow between the heat exchanger (HE) and the hydride, $\Delta H \left[\frac{\text{J}}{\text{mol}} \right]$ is the molar-based reaction enthalpy, and $M_{H_2} \left[\frac{\text{kg}}{\text{mol}} \right]$ is the molar mass of hydrogen.

The mass exchange between the hydride and the connected gas network is also performed by applying the mass conservation law. The hydride tank is connected to a gas volume (gas network), which is defined by the following mass conservation Equation (4), based on the Simscape [29]:

$$V \frac{\rho_g}{p_g} \cdot \frac{dp_g}{dt} - V \frac{\rho_g}{T_g} \cdot \frac{dT_g}{dt} = \dot{m}_{port} - \dot{m}_{rate}, \quad (4)$$

where $V [\text{m}^3]$, $\rho_g \left[\frac{\text{kg}}{\text{m}^3} \right]$, $p_g \left[\frac{\text{kg}}{\text{m}^2 \text{ s}^2} \right]$, and $T_g [\text{K}]$ are the volume, density, pressure, and temperature of the gas volume, and $\dot{m}_{port} \left[\frac{\text{kg}}{\text{s}} \right]$ is the mass flow going/coming through the gas-connection port.

The energy conservation equation for the gas phase is defined by Equation (5):

$$V \left(\frac{h_g}{Z R T_g} - 1 \right) \cdot \frac{dp_g}{dt} + V \rho_g \left(c_p - \frac{h_g}{T_g} \right) \cdot \frac{dT_g}{dt} = \phi_{Port} + \dot{Q}_H + \dot{Q}_m, \quad (5)$$

where $h_g \left[\frac{\text{J}}{\text{kg}} \right]$ is the specific enthalpy of the gas, $Z [-]$ is the compressibility factor, $R \left[\frac{\text{J}}{\text{kg K}} \right]$ is the specific gas constant, and $\phi_{Port} \left[\frac{\text{J}}{\text{s}} \right]$ is the energy flow in the gas connection point of the gas volume. \dot{Q}_H represents the heat exchange between the volume and the environment. $\dot{Q}_m \left[\frac{\text{J}}{\text{s}} \right]$ is a correction term that prevents changes in the temperature of the gas volume, according to assumption 7. This correction mass flow term \dot{Q}_m is based on the $\dot{m}_{R.rate}$ and defined with Equation (6):

$$\dot{Q}_m = \dot{m}_{rate} \left(\frac{h_g p_g}{Z R T_g \rho_g} - \frac{p_g}{\rho_g} \right). \quad (6)$$

As mentioned in assumption 3, hydrogen is treated as an ideal gas by applying the ideal gas equation of state (7):

$$p_g V = Z \frac{\rho_g V}{M_{H_2}} R T_g. \quad (7)$$

3.1.1. Thermodynamics of the Metal Hydride: Determination of the Equilibrium Pressure through Pressure-Composition-Isotherms (PCIs) Modeling

Determining the equilibrium pressure (p_{eq}) of the hydride formation and decomposition is critical to model the behavior of hydrides. In this regard, room temperature hydrides usually present pressure compositions isotherms (PCIs) with a steep slope and large hysteresis. The cause of PCIs with slope can be attributed to the H-H interaction, since the space lattice does not continuously increase with the hydrogen concentration [30]. The hysteresis of the PCIs is a reversible process attributed to the coherent strain energy caused by the interstitial hydrogen uptake and release upon the hydrogenation and dehydrogenation processes [31,32].

The industrially produced TiFeMn powder used in this work presents a strong slope in the plateau region and hysteresis between the absorption and desorption curves. The application of the van't Hoff equation for the calculation of the p_{eq} is not entirely representative of the thermodynamic behavior of the hydride since it does not consider the plateau slope [33]. Therefore, a mathematical function based on the one proposed in [34] was developed. This function depends on temperature T and hydrogen loading wt.%. The function developed for the absorption equilibrium pressure curves is defined in Equation (8):

$$p_{eq,abs} = c_a \left(T e^{\left(\frac{a_{0,a}}{T} + a_{1,a} T + a_{2,a} T^2 + a_{3,a} w + a_{4,a} w^2 + a_{5,a} w^3 \right)} + e^{(b_{0,a} T + b_{1,a} T^2 + b_{2,a} T w + b_{3,a} w + b_{4,a} w^2)} + e^{(100 (w - b_{5,a}))} \right) + f_{kor,a1}(w), \quad (8)$$

with

$$f_{kor,a1}(w) = k_{1,a} e^{k_{2,a} w}, \quad (9)$$

and desorption equilibrium pressure curves are defined by the Equation (10):

$$p_{eq,des} = (c_d e^{\left(\frac{a_{0,d}}{T} + a_{1,d} T + a_{2,d} T^2 + a_{3,d} w + a_{4,d} w^2 + a_{5,d} w^3 \right)} + e^{(b_{0,d} T + b_{1,d} T^2 + b_{2,d} T w + b_{3,d} w + b_{4,d} w^2)} + e^{(100 (w - b_{5,d}))} + f_{kor,d1}(w)) f_{kor,d2}(w), \quad (10)$$

with

$$f_{kor,d1}(w) = k_{1,d} e^{k_{2,d} w}, \quad (11)$$

$$f_{kor,d2}(w) = \frac{1}{k_{3,d} e^{k_{4,d} w} + 1}. \quad (12)$$

In Table 2, it is possible to see all the coefficients for the p_{eq} pressure of absorption and desorption functions.

Table 2. Coefficients for absorption and desorption equilibrium pressure functions.

Coefficients	Absorption	Desorption	Coefficients	Absorption	Desorption
a_0	-2.8724×10^3	-1.6692×10^3	b_3	2.7672×10^{-1}	-6.2484
a_1	2.0849×10^{-2}	1.434×10^{-2}	b_4	6.1852×10^{-1}	4.3904
a_2	-2.5888×10^{-5}	4.6251×10^{-6}	b_5	1.7878	1.5578
a_3	9.4389	9.0343	c	0.1667	0.2128
a_4	-9.7116	-7.9554	k_1	8.5869×10^{-12}	1.2417×10^{-69}
a_5	3.4163	2.5782	k_2	1.8013×10^1	1.0428×10^2
b_0	1.2467×10^{-2}	1.8402×10^{-2}	k_3		2.9935×10^{-3}
b_1	-3.2360×10^{-5}	-5.181×10^{-5}	k_4		3.8364
b_2	3.6551×10^{-3}	4.2442×10^{-3}			

These equations cover the full range of experimental temperatures and pressures used in this work.

The coefficients a_x and b_x were calculated using the curve fitting tool of MATLAB, which uses a trust-region procedure. For this purpose, experimental PCI data points measured in the context of the HyCare project were fitted [26]. An annealed TiFeMn alloy with the same composition as the one used in this work was employed for the PCIs measurements.

As mentioned in Section 2.2.1 Scenario A, the MH-tanks reached a capacity of 1.54 wt.% H₂ at room temperature and final pressure of 40 bar (ESI, Figure S1: Loading of all tanks at room temperature, ~20 °C, and up to 40 bar). To ensure that the function for calculating the equilibrium pressure with the coefficients from Table 2 reaches a loading of 1.54 wt.% at ~20 °C and 40 bar, a correction function must be introduced. Therefore, it was necessary to introduce the term f_{kor} for the proper fitting of the absorption and desorption PCIs, so that the fitted curves at 40 bar reach the loading 1.54 wt.% H₂. This correction factor $f_{kor,1}(w)$ was introduced, so it acts on the PCIs' fitted of hydrogenation from about 1.4 wt.% H₂. Therefore, from 0 wt.% H₂ to about 1.4 wt.%, the fitted PCI functions match very well with the measuring points without any correction factor.

The equilibrium pressure functions for dehydrogenation, in the temperature range from 0 °C to 20 °C and within the loading range of 1.3–1.54 wt.%, provide much higher p_{eq} values than the experimentally measured ones. Therefore, another term $f_{kor,2}(w)$ was introduced to correct this deviation (Equation (12)).

Figure 3 illustrates the experimental and fitted PCI curves. As demonstrated, there is an excellent agreement between the experimental data and the developed model. It is also important to mention that, in the context of the experiments carried out in this work, only the desorption case occurs.

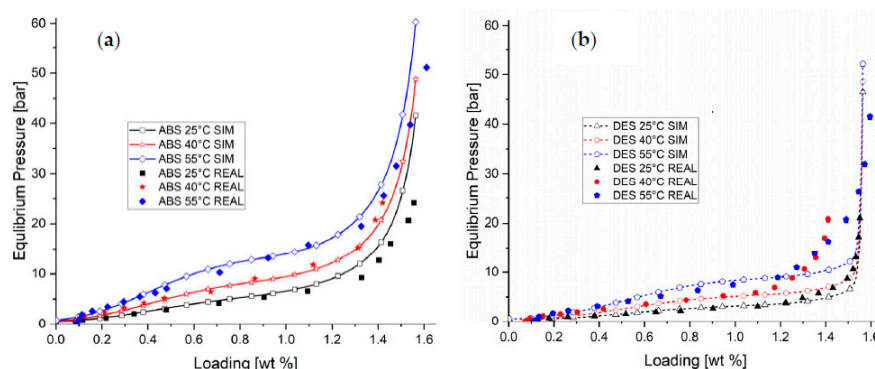


Figure 3. Comparison between the experimental (symbols) and fitted PCIs for TiFeMn hydride forming alloy (lines). Solid lines illustrate fits for the absorption (a) and dotted lines, desorption (b).

3.1.2. Kinetics of the Metal Hydride: Reaction Kinetic Model

The applied model for the reaction kinetic behavior was obtained from [21]. Equations (12) and (13) describe the expressions for the hydrogenation and dehydrogenation rates, respectively:

$$\dot{m}_{rate,Abs} = C_a \cdot \exp\left(-\frac{E_a}{RT_m}\right) \cdot \frac{p_g - p_{eq}}{p_{eq}} \cdot (\rho_{max} - \rho_s), \quad (13)$$

$$\dot{m}_{rate,Des} = C_d \cdot \exp\left(-\frac{E_d}{RT_m}\right) \cdot \frac{p_g - p_{eq}}{p_{eq}} \cdot (\rho_s - \rho_{min}), \quad (14)$$

where $E_a \left[\frac{J}{mol}\right]$ and $E_d \left[\frac{J}{mol}\right]$ are the activation energies, and $C_a \left[\frac{1}{s}\right]$ and $C_d \left[\frac{1}{s}\right]$ are the reaction constants for absorption and desorption, respectively. $\rho_s \left[\frac{kg}{m^3}\right]$ is the crystalline density of the alloy, and $\rho_{max} \left[\frac{kg}{m^3}\right]$ and $\rho_{min} \left[\frac{kg}{m^3}\right]$ are the maximum and minimum crystalline densities.

The experimental measurements of the MH2-Powerbank were performed under dynamic conditions (i.e., far away from the equilibrium conditions). Therefore, the model represents such dynamic behavior, and the conditions described in Equations (15)–(17) must be fulfilled for the hydrogen absorption or release to happen:

$$\text{if } p_g > p_{eq,Abs} \rightarrow \text{Absorption process occurs}, \quad (15)$$

$$\text{if } p_g < p_{eq,Des} \rightarrow \text{Desorption process occurs}, \quad (16)$$

$$\text{otherwise } \dot{m}_{rate} = 0. \quad (17)$$

These conditions also account for the zero mass flow of hydrogen when the gas pressure is in the hysteresis range.

3.1.3. Heat Exchange Modeling: Dehydrogenation of MH-Tanks by Utilizing the Fuel Cell Waste Heat

The heat exchange between the MH-tanks and the heat exchanger (exhaust air of the fuel cell) is described via steady-state heat transference, applying Equation (18):

$$\dot{Q}_{HE} = \frac{1}{\left(\frac{d_3}{d_2} \frac{1}{\alpha_s} + \frac{d_3}{d_2} \frac{1}{\alpha_{s-w}} + \frac{1}{\alpha_w} + \frac{1}{\alpha_{w-Air}}\right)} A (T_m - T_{Air}), \quad (18)$$

where α_s , α_{s-w} , α_w , and α_{w-Air} are the heat transfer coefficients inside the hydride bed, between the hydride bed and the internal tank wall, inside the tank wall, and between the tank wall and the air stream, respectively. These parameters are defined further below. $A \left[m^2\right]$ is the outer surface area, $T_m \left[K\right]$ is the equilibrium temperature of the gas and solid phases and T_{Air} is the temperature of the heat exchange fluid. The length taken to model the internal conduction of the MH-tanks is radial, and all the distances are referred to the center of the cylindrical geometry. The diameter d_1 is defined to describe the heat conduction path inside the hydride bed of the tanks. Figure 4 describes the distances inside the radial cross-section of an exemplary tank (Figure 4a) and the geometrical disposition of the 5 tanks inside the heat exchange housing (Figure 4b).

Equation (19) illustrates the definition of the effective thermal conductivity inside the hydride bed in the radial direction (α_s):

$$\alpha_s = \frac{2 \lambda}{d_2 \ln\left(\frac{d_2}{d_1}\right)}, \quad (19)$$

with

$$\lambda = \lambda_s(T) (1 - \epsilon) + \lambda_g(p, T) \epsilon, \quad (20)$$

where $\lambda_g(p, T)$ is the thermal conductivity of the hydrogen, and it is evaluated as a function of the temperature T and pressure p by the 2-dimensional interpolated table lookup function of Simulink. The data used for the determination of λ_g was obtained from [35]. Furthermore, the λ_g as a function of temperature and pressure is provided in ESI-Table S1. The conductivity of the solid λ_s is determined by linear function through 25 °C and 100 °C from the data taken [21].

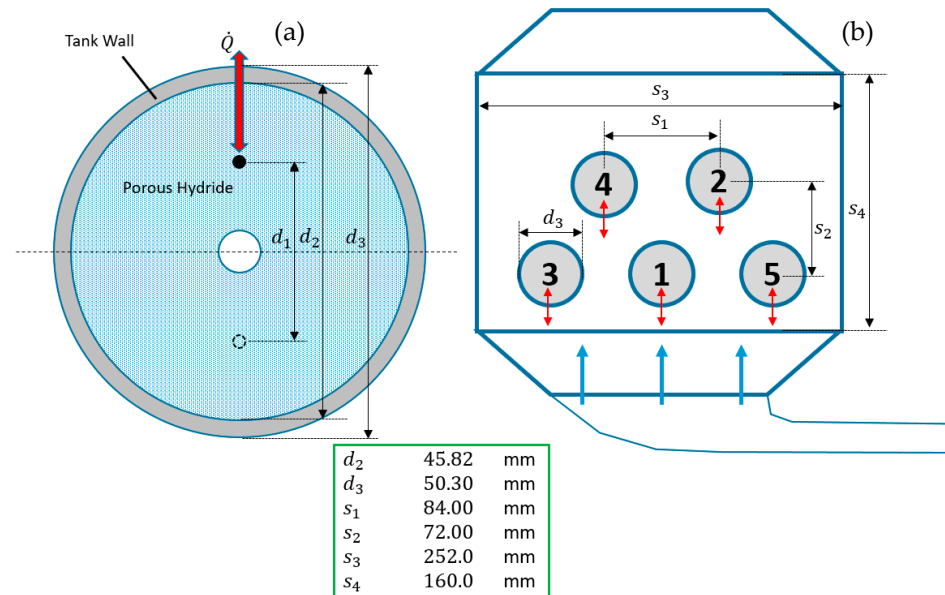


Figure 4. Heat transfer radial lengths in the internal cross-section of a tank (a) and disposition of the cylinders bundle inside the heat exchange housing (b).

The heat transfer coefficient α_{s-w} is determined experimentally by applying a calibration procedure. The calibration coefficient consisted of fitting the measured temperature curve corresponding to tank 3 (illustrated in Figure 4). Thus, a value of $\alpha_{s-w} = 10.21 \frac{\text{W}}{\text{m}^2 \text{K}}$ was obtained. The airflow in tank 3 was considered higher than in the other tanks. Thus, a correction factor was applied for the determination of α_{s-w} for the other tanks due to the high airflow. In this way, the experimental calibration curves demonstrated good agreement with the calculated curves.

The heat transfer through the vessel wall of steel (α_w) is described by the heat conduction. Therefore, the following applies to the heat transfer coefficient:

$$\alpha_w = \frac{2 \lambda_{St}}{d_3 \ln\left(\frac{d_3}{d_2}\right)}, \quad (21)$$

where λ_{St} is the thermal conductivity of steel.

The heat transfer between the wall and the air α_{w-Air} for the tube bundle is defined as illustrated in Equation (22) and depends on the air exhaust velocity $v_A \left[\frac{\text{m}}{\text{s}}\right]$ coming from the fuel cell. The α_{w-Air} coefficient is calculated according to the procedure described in [36].

$$\alpha_{w-Air} = \frac{Nu_{bundl} \lambda_{Air}}{l}, \quad (22)$$

where $\lambda_{Air} \left[\frac{\text{W}}{\text{mK}}\right]$ is the thermal conductivity of the air, l [m] is the overflow length of a single cylinder with $l = \frac{\pi}{2} d_3$ and the mean Nusselt number Nu_{bundl} of a cross-flowed plain tube bundle (Figure 4b), where velocity v_A is considered. A detailed description of the equations applied for the α_{w-Air} can be found in the ESI.3: Calculation of the heat transfer coefficient between the wall and the air α_{w-Air} for the tube bundle.

3.1.4. Model Implementations in Simscape

Figure 5 describes the conceptual implementation of the model in the platform Simscape. The grey cylinders represent the MH-tanks modeled in Simulink according to the physical background described in Sections 3.1.1 and 3.1.2. The yellow boxes represent the heat exchange model implemented in Simulink, as explained in Section 3.1.3. MH-tanks are assembled via a gas reservoir interphase of Simscape (blue box, modified constant volume chamber), applying the mass conservation Equation (4) to create a connection to the fuel cell with mass flow $\dot{m}_{BZ}(t)$. As illustrated, the pipes (Figure 5, blue cylinders) are also represented and interconnected. The air velocity around each tank and coming from the exhaust of the fuel cell is represented by $v_{T1-T5}(t)$. $T_A(t)$, and $v_A(t)$ represents the temperature and velocity measured in the anemometer (Figure 1a).

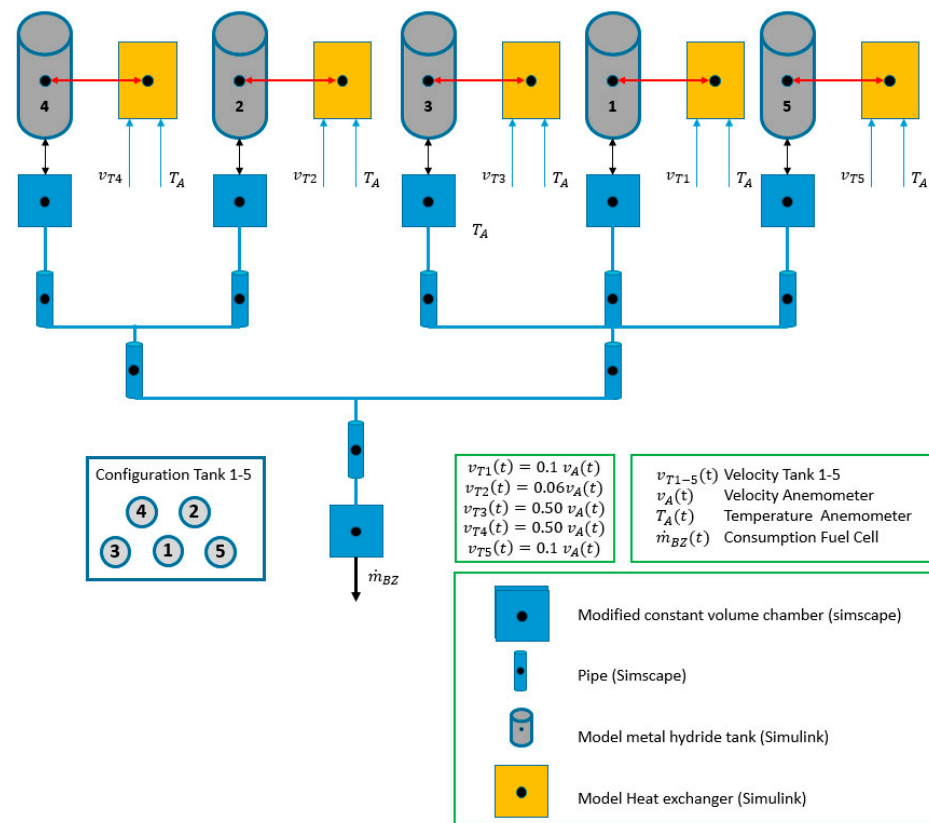


Figure 5. Implementation of MH2-Powerbank in MATLAB Simulink/Simscape: regulation of the air velocity.

The 0D model of the MH-tanks (Figure 5, grey cylinders) is implemented through the mass and heat conservation Equations (1) and (2) in the hydride phase, respectively. The model for the heat exchanger (Figure 5, yellow boxes) is integrated into the system via the energy exchange equation in steady-state, described by Equation (18). The air velocity is determined from data obtained from the anemometer and according to the procedure described in ESI.4: Determination of the airspeed of the fuel cell exhaust air. Due to the design of the heat exchanger, the heat exchange of tanks 3 and 4 is significantly better than in the other tanks. Thus, a correction factor is applied to the velocities as seen in the velocity equations in each $v_{T1-T5}(t)$ (Figure 5). The determined air velocities are used for the determination of the α_{w-Air} coefficient, as described in Section 3.1.3.

In the case of the modified constant volume chamber (Figure 5, blue box), the mass and energy conservation Equations (4) and (5), respectively, for the interconnection of the components are applied.

For the simulation of the pipe-system, the Simscape component “pipe (G)” is used, which is described in ESI.5 [37].

3.1.5. Boundary Conditions

The measured profiles of hydrogen consumption, fuel cell exhaust airflow velocity, and temperature set the model boundary conditions. These profiles were measured according to the described scenario C, Section 2.2.1. The experimental profiles measured at 5.0, 7.5, 10.0, and 20.0 Ohm, dynamic daily profiles, and large power consumption variations are provided in ESI.6 to 8 (Figure S3, Hydrogen consumption, Figure S4, Interpolated air velocity profiles, and Figure S5, Interpolated temperature profiles. The interpolated temperature profiles of the 5, 10, and 20 Ohm experiments are used in [38]). In order to introduce the boundary conditions based on the experimental results operation conditions of the fuel cell, the measured values are interpolated to define time function dependences.

Figure 6 demonstrates exemplary results from a test carried out at 5 Ohm. It is possible to observe the mass consumption of the fuel cell \dot{m}_{BZ} (Figure 6a), the velocity measured in the anemometer v_A (Figure 6b), and the measured and the modified air temperature T_A (Figure 6c,d).

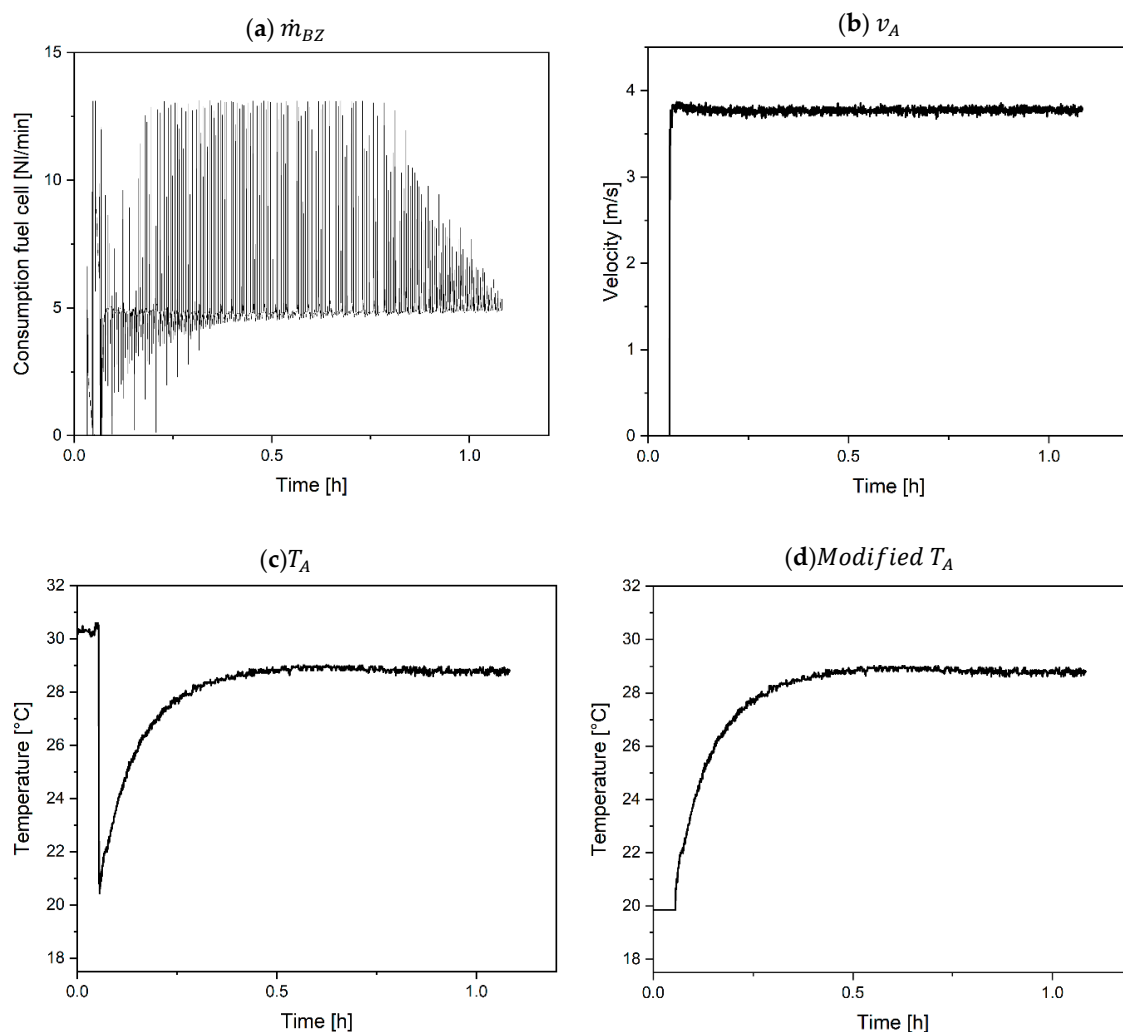


Figure 6. Experimental measurements to set the boundary conditions for the hydride storage and gas network models: (a) Fuel cell consumption, (b) Air velocity of the exhaust gas from the fuel cell, (c) Air temperature, and (d) Modified air temperature of the airflow coming from the fuel cell.

All hydrogen consumption profiles of the fuel cell present the same behavior, as demonstrated in Figure 6a. This behavior is characterized by a high number of peaks caused by the so-called “purging” of the fuel cell. Inside the FC, a valve is opened to allow a pressure purge to remove impurities from the anodic side of the fuel cell during this

process. The height of the peaks reaches a maximum of 13.6 NL/min. Due to the hydrogen consumption of the fuel cell, the gas pressure in the MH-tanks decreases, which consequently reduces the differential pressure between the tanks and the ambient atmosphere. Thus, at about 0.7 h, the peak heights start to decrease. As the system approaches the ambient pressure, the consumption peaks are no longer visible in the profile. In the 5 Ohm experiment, the base consumption is approx. 5 NL/min. All profiles of consumption of the fuel cell can be found in ESI.5: Figure S2.

Figure 6b displays the air velocity measured by the anemometer. After about 0.1 h, the operation of the fan starts and generates a velocity of ~3.8 m/s. The velocity data obtained from the anemometer were defined as a function of time applying a linear interpolation between the values. These interpolated velocity profiles used in every experiment can be found in ESI.6: Figure S3.

Figure 6c demonstrates that the measured temperature of the air stream reaches values above 30 °C within the first 0.05 h. This observed temperature behavior is due to the fan of the fuel cell not being active initially (see Figure 1a). This initial temperature behavior does not represent the fuel cell operative conditions. Therefore, the ambient temperature is used as the air temperature of the fuel cell waste heat for the simulation (Figure 6d) (i.e., after the fan is in an operative state). Due to the fuel cell operation, the temperature rises from about 18 °C to about 29 °C within 0.5 h. Then, the temperature remains relatively constant, until the end of the experiment. In ESI.7: Figure S5, all the interpolated temperature profiles from the fuel cell exhaust air stream are provided.

3.1.6. Initial Condition and Simulation Parameters

In Tables 3 and 4, the main initial conditions and parameters, respectively, for the simulation are described.

Table 3. Initial parameters for the MH-system.

Parameter	Value	Unit	Description
$T_{m,0}$	From 17 to 21	°C	Range of initial measured temperature for the tanks
$\rho_{s,0}$	3250.04	$\frac{\text{kg}}{\text{m}^3}$	Initial crystalline density full load (considering the experimental gravimetric capacity: 1.54 wt.%)
$P_{g,0}$	40	bar	Initial gas pressure under hydrogenated state.

Table 4. Material, kinetic, and thermal parameters for the MH-system [21,39].

Parameter	Value	Unit	Description	Parameter	Value	Unit	Description
k_{abs}	2.6536	$\frac{1}{\text{s}}$	Reaction kinetic constant of abs.	ΔH_{Abs}	From −33,638 to −28,211	$\frac{\text{J}}{\text{mol H}_2}$	Enthalpy of abs. in the range of 0.2–1.3 wt.%
k_{Des}	0.8852	$\frac{1}{\text{s}}$	Reaction kinetic constant of des.	ΔH_{Des}	From −34,917 to −29,969	$\frac{\text{J}}{\text{mol H}_2}$	Enthalpy of des. in the range of 0.2–1.3 wt.%
E_{Abs}	17,500	$\frac{\text{J}}{\text{mol H}_2}$	Activation energy of abs.	$\rho_{s,min}$	3200	$\frac{\text{kg}}{\text{m}^3}$	Minimal bulk density
E_{Des}	13,750	$\frac{\text{J}}{\text{mol H}_2}$	Activation energy of des.	$\rho_{s,max}$	3250.04	$\frac{\text{kg}}{\text{m}^3}$	Maximal bulk density
c_s	682.4	$\frac{\text{J}}{\text{kg K}}$	Heat capacity	ϵ	0.5	—	Porosity
$\lambda_s(T)$	5–6.2	$\frac{\text{W}}{\text{m K}}$	Thermal conductivity solid	$\lambda_g(p, T)$	0.163–0.227	$\frac{\text{W}}{\text{m K}}$	Thermal conductivity gas [39]

4. Model Validation and Discussion of the Results

This section illustrates the experimental tests performed according to the operating scenario C (Section 2.2.1) and experimental parameters (Section 2.2.2). Three different scenarios are illustrated: constant charge (experiments 1–4 in Table 1), high power loads and dynamic loads (experiment 5 in Table 1, Section 2.2.2), and daily dynamic power loads (experiment 6 in Table 1). Such experimental results are compared with the developed

system model and the outcomes discussed. These GtoP scenarios allow for investigating the behavior of the MH2-Powerbank system in the case of power outages.

The MH-tanks system was cycled several times to carry out the experiments, demonstrating stable cycling behavior. Eleven hydrogenation and dehydrogenation cycles were performed during the hydride forming alloy's activation (2 cycles), and all performed tests (some of them are not included in this paper). During the activation, the system's maximum capacity is 1.54 wt.% (110 g of H₂). However, depending on the experimental conditions upon hydrogen provision, supplied hydrogen capacity ranged between 0.5 and 1.0 wt.%. No deterioration of the hydrogen storage capacity of the system was noticed during cycling.

Figure 7 illustrates the temperature and pressure experimental and simulation profiles from tanks 1 and 3 for the fuel cell representative operation at 5.0 Ohm (Figure 7A) and 10.0 Ohm (Figure 7B). These representative scenarios were considered since the behavior under the other resistances conditions of the fuel cell is similar. Further results from tanks 2, 3, and 5 can be viewed in the ESI.9: Figure S6 and ESI.10: Figure S7, respectively.

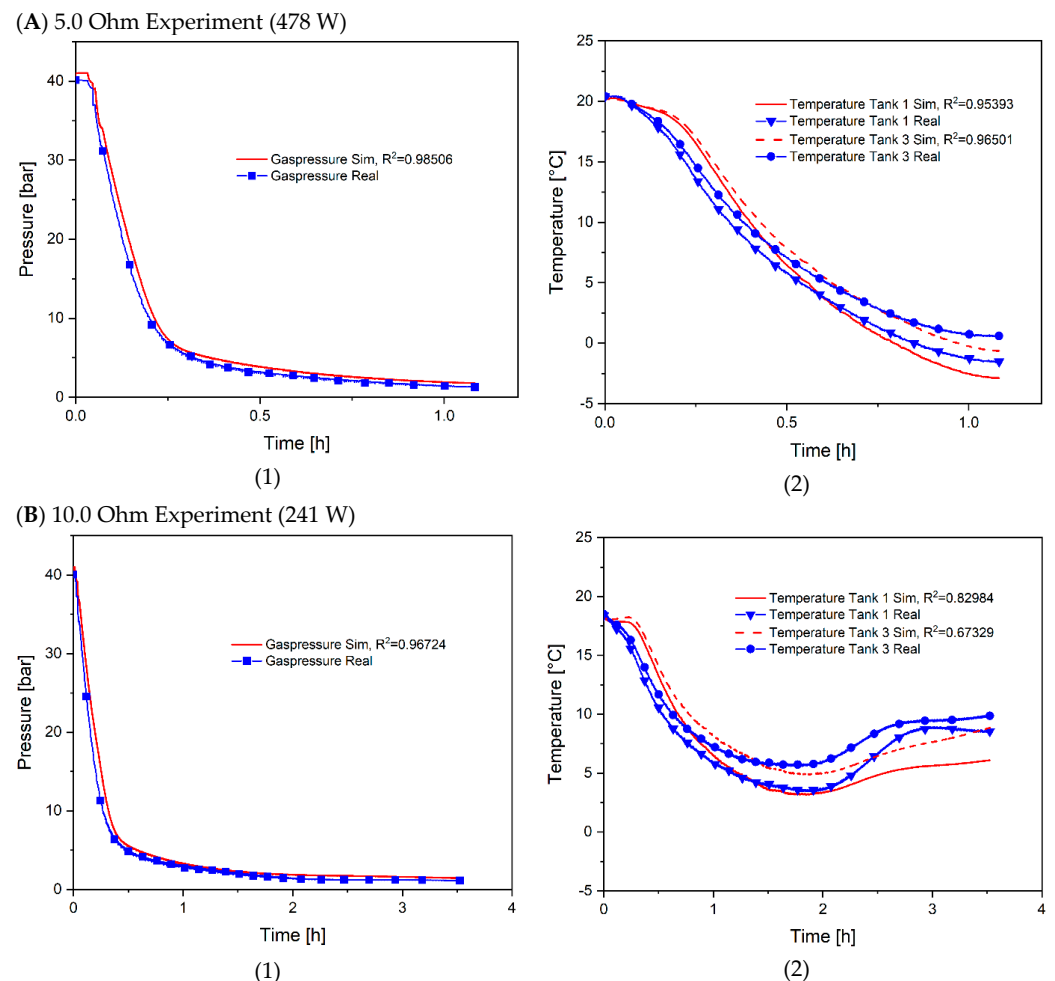


Figure 7. Simulated (Sim) and measured (Real) system pressure curves (1) and temperature curves of tanks 1 and 3 (2) at different conditions: (A) 5.0 Ohm and (B) 10.0 Ohm experiments.

For the scenario under a constant resistance of 5.0 Ohm (Figure 7(A1)), the pressure curve starts at 40 bar and decreases, due to the baseline consumption of the fuel cell of about 5 NL/min (see Figure 6a) within 0.23 h to 6.23 bar. Subsequently, the slope of the curve drops sharply, so that by the end of the experiment, only a pressure decrease of 5.15 bar to the nearly ambient pressure of 1.08 bar occurs during 1.2 h, while a total amount of hydrogen of about 0.4 wt.% H₂ was desorbed.

The observed substantial pressure drop (Figure 7(A1)) is mainly due to the hydrogen removal from the gas phase of the tanks: the system pressure is clearly above the plateau pressure of the hydride at about room temperature (see Figure 3). In addition, the mass flow consumed by the fuel cell is the highest at the beginning, because of the considerable pressure difference between the system pressure (40 bar) and the fuel cell supply pressure (ambient pressure of 1.013 bar). Due to this difference, the fuel cell purging causes a more significant hydrogen consumption (see Figure 6a). As soon as the pressure drops below the desorption plateau (about 6.2 bar, see Figure 3), the pressure driving force increases further. Hence, a more significant hydrogen amount is desorbed from the hydride, reducing the slope of the pressure curve strongly until reaching 1.08 bar (final pressure). In addition, the decreasing system pressure also reduces the mass flow caused by the purging, so that the desorption rate decreases as well (see also Figure 6a): after about 0.75 h, the amplitude of the purging peaks decreases from about 13.6 NL/min steadily until they are no longer visible and reach the baseline consumption of about 5 NL/min.

The same curve characteristics are also evident in the temperature curve of Figure 7(A2). In tank 1, the temperature decreases from an initial 20 °C to −2.12 °C within 1.2 h, because of the endothermic desorption reaction. It can be observed that the temperature curve gradient increases within the first 0.5 h and then decreases until the end of the experiment, where it displays a flat fraction and reaches a temperature of −2.12 °C. At this point, the heat input through the heat exchanger is identical to the desorption reaction energy flow. In the case of tank 3, it only reaches a temperature of 0.68 °C. The temperature curves of the different tanks differ because the waste heat from the fuel cell is not evenly distributed to the tanks, as mentioned above.

In Figure 7(B1), the characteristic pressure curve is identical to the previous one. Again, the system pressure drops sharply from 40 bar to about 6 bar within the first 0.4 h and then continues with a smaller slope. In contrast to the previous experiment, however, the fuel cell can be operated for a much longer time (3.6 h). Moreover, a more significant amount of hydrogen of about 0.8 wt.% is desorbed from the tanks.

Due to the reduced baseline consumption of 2.6 NL/min, compared to the 5.0 Ohm experiment (see ESI.5: Figure S2), the temperature decrease in the tanks is less pronounced. Minimum temperature values of 3.57 °C after 1.9 h and 5.68 °C after 1.8 h are reached in tanks 1 and 3, respectively. The temperature drop to the minimum value is due to the endothermic desorption reaction. In tank 1, the reached minimum temperature level is lower, because the heat exchange with the waste heat airflow of the fuel cell is not as effective as in tank 3. In this regard, the temperature profiles in the last measurement stage (Figure 7(B2)) do not present the same behavior. For both tanks, the temperature rises after 3 h: 8.9 °C for tank 1 and 9.0 °C for tank 3. The observed temperature increase is caused by the reduced consumption of the fuel cell (see Figure 6a). Under reduced hydrogen consumption conditions, the rate of energy demand for the tank to provide hydrogen decreases, and the energy provided by the heat exchanger heats the tanks. In the case of tank 3, the temperature remains stable at 9.0 °C. However, the temperature in tank 1 drops again to 8.6 °C after 3.5 h. This temperature drop is related to the dehydrogenation of the central part of the tank, where the thermocouple is placed. Thus, in the middle of the hydride bed, the heat transfer is not as effective as the hydride bed contact with the outer shell. As soon as the reaction takes place more in the area around the thermocouple, a slight temperature drop is registered, as displayed in Figure 7(B2).

The lower temperature decrease for the experiment at 10.0 Ohm (Figure 7B) compared to the experiment carried out at 5.0 Ohm (Figure 7A) account for the significant increase of hydrogen desorbed: 0.4 wt.% at 5.0 Ohm and 0.8 wt.% at 10.0 Ohm. At higher temperature levels, the equilibrium pressures are higher (see Figure 3), resulting in a more significant driving force and improved kinetic behavior.

The simulation results provided in Figure 7A,B are in good agreement with the experimental results. On the one hand, the high degree of correlation of the system model for the pressure profiles is based on the realistic representation of the variation of the equilibrium

pressure with the hydrogen concentration and temperature, as expressed by the developed model (Equation (10)). On the other hand, the experimental calibration of the heat transfer coefficient α_{s-w} provided in Equation (18) allowed for modelling the temperature profiles with a reasonable degree of correlation, since the last stages of the curves present a more significant deviation from the modeled curves. These deviations are ascribed to the decrease mentioned above in fuel cell consumption and the heat transfer distribution.

M. Gambini et al. [40] developed a 0D model based on mass and energy conservation to simulate the de-/hydrogenation of MH-tanks. This model was able to simulate the essential dynamics in the absorption and desorption of MH-tanks. It was validated by using the data from P. Muthukumar et al. [41] by comparing it with experimental results from two MH-tanks containing 0.5 kg of $\text{MmNi}_{4.6}\text{Al}_{0.6}$ and $\text{MmNi}_{4.6}\text{Fe}_{0.6}$ low-temperature hydrides. These tanks were individually desorbed from a 30–35 bar pressure to ambient pressure of 1 bar. The heat exchange was done using a liquid medium instead of air, as in this work. Despite the different hydrides, different kinds of configuration, and cooling medium, the experimental results of the temperature and pressure profiles demonstrate similar characteristics, as illustrated in Figure 7. However, the temperature drop behavior observed for tank 1 at 10 Ohm for the last measurement stage (Figure 7(B2)) represents a deviation from the behavior reported in [40].

In Figure 8, the system is operated with a high load change between 149 W and 596 W, as described in scenario C, Section 2.2.1. These experiments aim to test whether strong fluctuations in the load (e.g., in the case of highly fluctuating consumers) pose a problem for the fuel cell.

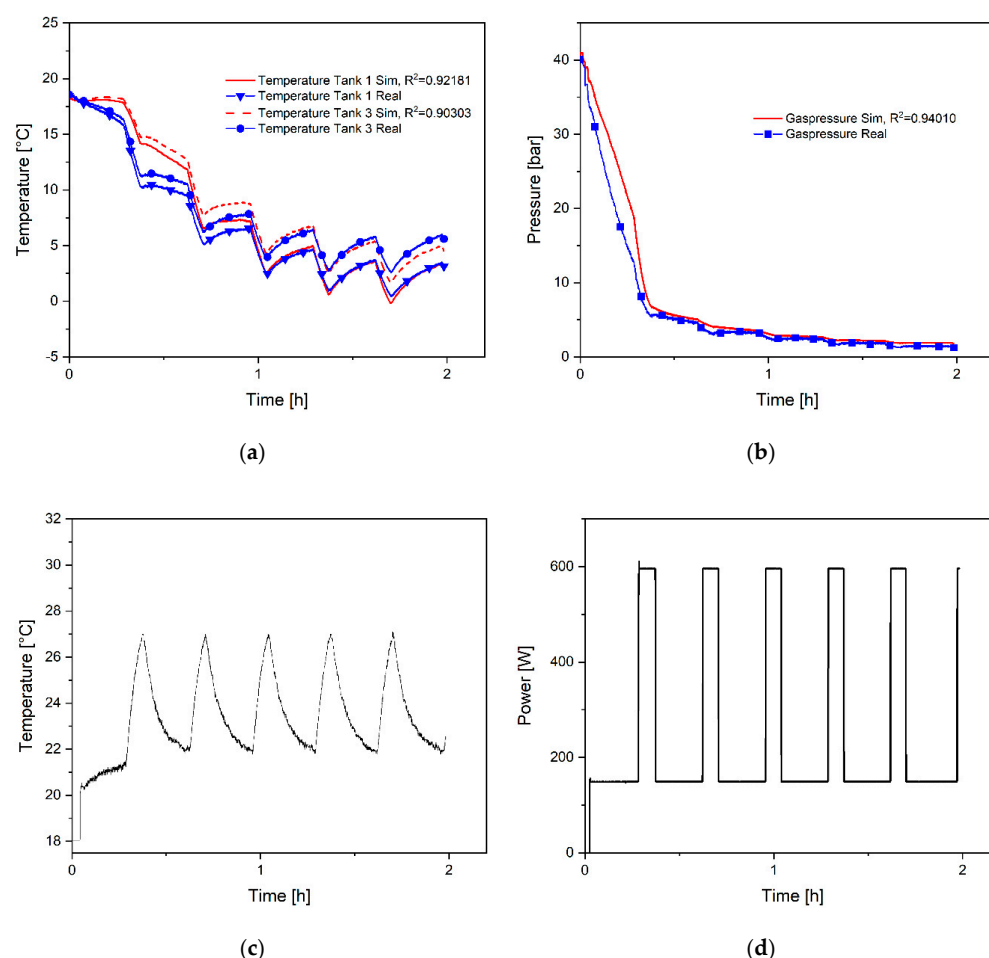


Figure 8. Variable high load conditions: (a) Simulated (Sim) and measured (Real) temperature development of tanks 1 and 3, (b) Simulated (Sim) and measured (Real) system pressure, (c) temperature of air stream from the fuel cell, and (d) power of the fuel cell.

Figure 8a illustrates the temperature curve of tanks 1 and 3. The temperatures of these tanks drop from about 18 °C to 16 °C in the first 15 min. Subsequently, the absolute value of the slope increases and the temperature drops to about 10 °C within 5 min. In the following steps, the temperature of the tank displays a fluctuating behavior until the end of the experiment (1.9 h). This behavior is caused by the change of the power setting of the fuel cell and thus its hydrogen consumption. In the first 15 min, a baseline value of 1.6 NL/min is consumed at a load of 149 W. Then, a higher power load of 596 W for 5 min is set, and consequently, the consumption increases to 5.5 NL/min. The described load variation between 149 W and 596 W is repeated until the end of the experiment. Due to the substantial load at 596 W, after 1 h, the air stream temperature coming from the fuel cell increases from about 22 °C to 27 °C within 5 min, as illustrated in Figure 8c. Although the power is then reduced to 149 W and the air stream temperature from the fuel cell starts to decrease (Figure 8c), the temperature in the MH-tanks still increases (Figure 8a). Therefore, the MH-tanks dehydrogenation process benefits from the fuel cell temperature increase by accelerating the kinetic behavior.

Figure 8b illustrates the system pressure drop curve under the high-varying-power load. As demonstrated, the system pressure does not decrease as smoothly as in the case of the constant power load (Figure 7A,B). The system pressure curve displays slight slope changes related to the power load changes during the test. The hydrogen storage capacity consumed by the large variable loads of the fuel cell lies at about 0.47 wt.%. As demonstrated, the decrease to lower loads (i.e., 150 W) allows for reaching a temperature level so that the provided capacity is larger than the capacity of the stable load condition at 478 W with 5 Ohm resistance (0.4 wt.%, Figure 7A).

For this particular dynamic high power load condition, the system simulations also demonstrated a fairly good correlation with the experimental results, as illustrated by the values of the fitting goodness parameters (Figure 8a,b). It is also interesting to compare the MH-system response, in terms of temperature and pressure, with other tests that simulate highly variable loads, such as vehicular driving cycles [42]. In this case, the sudden variations in the hydrogen flow result in a temperature behavior, which is analogous to the behavior displayed in Figure 8a.

A further test was carried out to prove whether the system could provide sufficient energy during daily dynamic load changes, as described in scenario C, Section 2.2.1. This scenario is essential to test the system for emergency power supply purposes. For this reason, a representative household scenario on Saturday afternoon in winter from 5:00 p.m. with an annual power consumption of 1000 kWh/year was chosen [27]. Figure 9 demonstrates the representative results of the temperature profiles from tanks 1 and 3 (Figure 9a), the system's pressure drop (Figure 9b), the temperature profile of the air stream coming from the fuel cell (Figure 9c), and fuel cell power (Figure 9d). As illustrated, the fuel consumption varies in small steps between the power requirements, from 149 W to a max of 215 W every 15 min (Figure 9d), which gradually leads to only minor changes in hydrogen consumption. The temperature profile of the air stream coming from the fuel cell displays a smooth behavior, ranging between about 21 °C and 23 °C (Figure 9c). In this scenario, the variation of the power load is not as substantial, as in the large power load variations (Figure 8). Therefore, the curves of temperature profiles of tanks 1 and 3 (Figure 9a) and the system's pressure drop (Figure 9b) are similar to those for constant load under 241 W with 10 Ohm, as illustrated in Figure 7B. Therefore, the MH2-Powerbank system under daily dynamic power load conditions behaves like a constant load system. In terms of hydrogen consumption from the fuel cell, about 0.76 wt.% was provided by the MH-system. This capacity is nearly similar to the one observed for stable loads at 10 Ohm (Figure 7B).

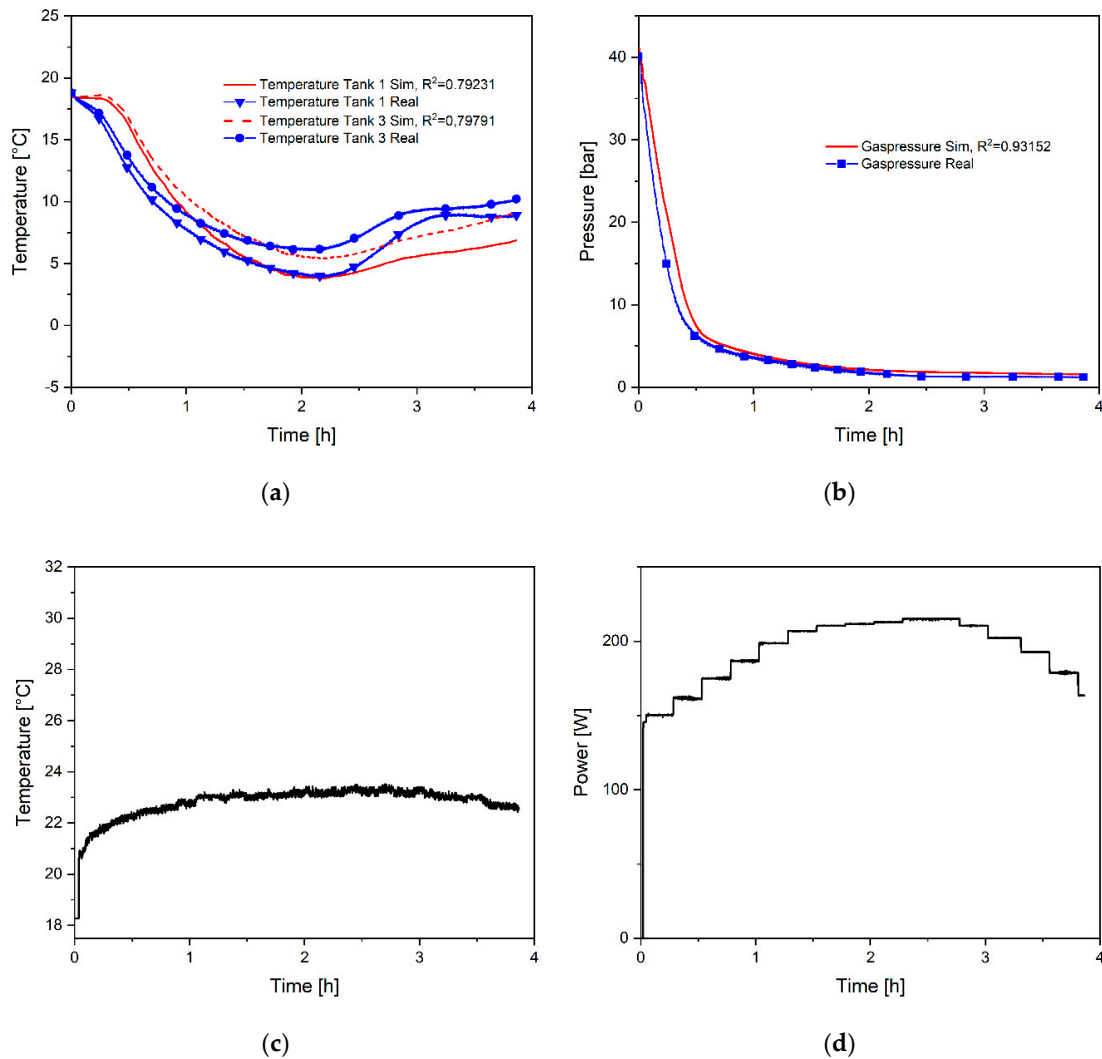


Figure 9. Variable dynamic load conditions: (a) Simulated (Sim) and measured (Real) temperature development of tanks 1 and 3, (b) Simulated (Sim) and measured (Real) system pressure (c), temperature of the air stream coming from the fuel cell, and (d) power of the fuel cell.

The system model is in good agreement with the experimental results in this scenario, particularly for the pressure profile (Figure 9b), and the differences between the experimental and simulated temperature profiles in the final stage of the test are the same as explained for the case exposed in Figure 7B.

5. Conclusions

The digital and experimental development of a gas-to-power system (GtoP) for power outages has been successfully demonstrated. Such a GtoP system, termed the MH2-Powerbank, is composed of a 1.6 kW air-cooled PEM fuel cell and a 6.7 kg TiFeMn based MH-system. The MH2-Powerbank can provide energy under different scenarios in a power range between 149–596 W. The waste heat from the air-cooled fuel cell is effectively utilized as a heat source for the dehydrogenation process of the MH-system. The tested dynamic consumption scenarios demonstrate that the concept of the MH2-Powerbank system is suitable for the emergency power supply of households due to its fast and reliable response to the power load changes.

A novel system modeling approach is also presented in this work. The developed 0D model, integrated into hydrogen-based gas networks using the MATLAB/Simscape library, demonstrates the advantages of low computational cost and full coupling between

the fuel cell and the MH-system. This modeling approach requires setting some boundary conditions by experimental calibrations and characterization of the hydride forming alloy and the heat transfer coefficient. The modeling of the MH2-Powerbank system displays an excellent agreement with the experimental results in all tested constant and dynamic power load scenarios. This work presents an experimental and digital strategy for integrating MH-systems in any hydrogen network for GtoP system applications and potential dimensioning.

Supplementary Materials: The following supporting information can be downloaded at <https://www.mdpi.com/article/10.3390/en15030844/s1>. Figure S1: ESI.1 Full loading MH2 Powerbank. Table S1: Loading of all tanks at room temperature of about 20 °C, and up to 40 bar. ESI.2 Hydrogen-Data for calculating the thermal conductivity coefficient of hydrogen as a function of pressure and temperature $\lambda_g(p, T)$. Figure S2: Thermal properties of air as a function of temperature and pressure: thermal conductivity λ [$\text{W m}^{-1} \text{K}^{-1}$] and thermal diffusivity a [$\text{m}^2 \text{s}^{-1}$]. ESI.3 Calculation of the heat transfer coefficient between the wall and the air α_{w-Air} for the tube bundle. ESI.4 Determination of the airspeed of the fuel cell exhaust air. ESI.5 Description of the “Pipe (G)” component in MATLAB/Simscape. Figure S3: Pipe (G) Simscape. ESI.6 Hydrogen consumption of the fuel cell used in the MH2-Powerbank. Figure S4: Hydrogen consumption of the fuel cell: experiments under constant resistance at 5.0, 7.5, 10.0, and 20.0 Ohm, dynamic daily profiles, and large power consumption variations. ESI.7 Interpolated velocity profiles from the fuel cell waste heat air stream obtained from the data measured with the anemometer. Figure S5: Interpolated velocity profiles from the fuel cell waste heat air stream: experiments under constant resistance at 5.0, 7.5, 10.0, and 20.0 Ohm, dynamic daily profiles, and large power consumption variations. ESI.8 Interpolated Temperature profiles from the fuel cell waste heat air stream obtained from the data measured in the anemometer. Figure S6: Interpolated Temperature profiles from the fuel cell waste heat air stream: experiments under constant resistance at 5.0, 7.5, 10.0, and 20.0 Ohm, dynamic daily profiles and large power consumption variations. ESI.9: Measured and simulated temperature profiles of tanks 1–5 from MH2-Powerbank. Figure S7: Experimental and modeled temperature profiles of the tanks under constant resistance at 5.0, 7.5, 10.0, and 20.0 Ohm, dynamic daily profiles, and large power consumption variations. ESI.10 Measured and simulated pressure profiles of MH2-Powerbank. Experimental and modeled pressure profiles of the tanks under constant resistance at 5.0, 7.5, 10.0, and 20.0 Ohm, dynamic daily profiles and large power consumption variations.

Author Contributions: Conceptualization, D.M.D., J.P. and J.J.; investigation, D.M.D.; resources, D.M.D. and M.C.G.; writing—original draft preparation, D.M.D., J.P. and T.-T.L.; writing—review and editing, D.M.D., J.P., J.J., T.-T.L., G.S., S.M., J.M.B.v.C., G.C. and T.K.; supervision, T.K., J.J., J.M.B.v.C., G.C., G.S. and S.M.; funding acquisition, T.K., J.J., G.S. and S.M. All authors have read and agreed to the published version of the manuscript.

Funding: This work was partially funded from the Fuel Cells and Hydrogen 2 Joint Undertaking (JU), under grant agreement No 826352, HyCARE project. The JU receives support from the European Union’s Horizon 2020 research, Hydrogen Europe, Hydrogen Europe Research, innovation programme and Italy, France, Germany, and Norway, which are all thankfully acknowledged. This work was also supported by a doctoral scholarship of the Hochschule Bonn-Rhein-Sieg, University of Applied Sciences.

Data Availability Statement: Data available on request due to restrictions e.g., privacy or ethical. The data presented in this study are available on request from the corresponding author. The data are not publicly available due to the regulations of data protection of the responsible institute.

Acknowledgments: Thanks go to Jürgen Stolzenberger for the great support with the programming in Labview, with which parts of the plant and the data acquisition were controlled. Thanks to the colleagues from the workshop at the Helmholtz-Zentrum hereon, who helped with the construction of MH2-Powerbank.

Conflicts of Interest: The authors declare no conflict of interest. The funders had no role in the design of the study, in the collection, analyses, or interpretation of data, in the writing of the manuscript, or in the decision to publish the results.

References

1. Forest, G.; Markova, A. *The Road to Carbon-Free Society*; Climate Change Energy and Environment; Friedrich Ebert Stiftung: London, UK, 2021. Available online: <http://library.fes.de/pdf-files/bueros/london/18473.pdf> (accessed on 22 December 2021).
2. Chitanava, M.; Janashia, N.; Samkhardze, I.; Vardosanidze, K. *The Impact of Climate Change Mitigation Policy on Employment*; Climate Basics; Friedrich Ebert Stiftung: Zagreb, Croatia, 2021. Available online: <http://library.fes.de/pdf-files/bueros/georgien/17558.pdf> (accessed on 22 December 2021).
3. Munta, M. *The European Green Deal*; Climate Change Energiy and Environment; Friedrich Ebert Stiftung: Zagreb, Croatia, 2020. Available online: <http://library.fes.de/pdf-files/bueros/kroatien/17217.pdf> (accessed on 22 December 2021).
4. Strunz, S.; Gawel, E.; Lehmann, P. The political economy of renewable energy policies in Germany and the EU. *Util. Policy* **2016**, *42*, 33–41. [\[CrossRef\]](#)
5. Egeland-Eriksen, T.; Hajizadeh, A.; Sartori, S. Hydrogen-based systems for integration of renewable energy in power systems: Achievements and perspectives. *Int. J. Hydrogen Energy* **2021**, *46*, 31963–31983. [\[CrossRef\]](#)
6. Gielen, D.; Boshell, F.; Saygin, D.; Bazilian, M.D.; Wagner, N.; Gorini, R. The role of renewable energy in the global energy transformation. *Energy Strategy Rev.* **2019**, *24*, 38–50. [\[CrossRef\]](#)
7. Yue, M.; Lambert, H.; Pahon, E.; Roche, R.; Jemei, S.; Hissel, D. Hydrogen energy systems: A critical review of technologies, applications, trends and challenges. *Renew. Sustain. Energy Rev.* **2021**, *146*, 111180. [\[CrossRef\]](#)
8. Muthukumar, P.; Groll, M. Metal hydride based heating and cooling systems: A review. *Int. J. Hydrogen Energy* **2010**, *35*, 3817–3831. [\[CrossRef\]](#)
9. Rusman, N.A.A.; Dahari, M. A review on the current progress of metal hydrides material for solid-state hydrogen storage applications. *Int. J. Hydrogen Energy* **2016**, *41*, 12108–12126. [\[CrossRef\]](#)
10. Bellosta von Colbe, J.; Ares, J.-R.; Barale, J.; Baricco, M.; Buckley, C.; Capurso, G.; Gallandat, N.; Grant, D.M.; Guzik, M.N.; Jacob, I.; et al. Application of hydrides in hydrogen storage and compression: Achievements, outlook and perspectives. *Int. J. Energy Res.* **2019**, *44*, 7780–7808. [\[CrossRef\]](#)
11. Aldas, K.; Mat, M.D.; Kaplan, Y. A three-dimensional mathematical model for absorption in a metal hydride bed. *Int. J. Hydrogen Energy* **2002**, *27*, 1049–1056. [\[CrossRef\]](#)
12. LExcellent, C.; Gay, G.; Chapelle, D. Thermomechanics of a Metal Hydride Tank. *Continuum Mech. Thermodyn.* **2014**, *27*, 379–397. [\[CrossRef\]](#)
13. Muthukumar, P.; Ramana, S.V. Numerical simulation of coupled heat and mass transfer in metal hydride-based hydrogen storage reactor. *J. Alloys Compd.* **2009**, *472*, 466–472. [\[CrossRef\]](#)
14. Kaplan, Y.; Veziroglu, T.N. Mathematical modelling of hydrogen storage in a LaNi₅ hydride bed. *Int. J. Energy Res.* **2003**, *27*, 1027–1038. [\[CrossRef\]](#)
15. Lahmer, K.; Bessaih, R. Impact of kinetic reaction models on hydrogen absorption in metal hydride tank modeling. *Int. J. Hydrogen Energy* **2015**, *40*, 13718–13724. [\[CrossRef\]](#)
16. Mohammadshahi, S.; Gray, E.; Webb, C. A review of mathematical modelling of metal-hydride systems for hydrogen storage applications. *Int. J. Hydrogen Energy* **2016**, *41*, 3470–3484. [\[CrossRef\]](#)
17. Lozano, G.A.; Na Ranong, C.; Von Colbe, J.M.B.; Bormann, R.; Fieg, G.; Hapke, J.; Dornheim, M. Empirical kinetic model of sodium alanate reacting system (II). Hydrogen desorption. *Int. J. Hydrogen Energy* **2010**, *35*, 7539–7546. [\[CrossRef\]](#)
18. Lozano, G.A.; Na Ranong, C.; von Colbe, J.M.B.; Bormann, R.; Hapke, J.; Fieg, G.; Klassen, T.; Dornheim, M. Optimization of hydrogen storage tubular tanks based on light weight hydrides. *Int. J. Hydrogen Energy* **2012**, *37*, 2825–2834. [\[CrossRef\]](#)
19. Jana, S.; Muthukumar, P. Design and Performance Prediction of a Compact MmNi_{4.6}Al_{0.4} based Hydrogen Storage System. *J. Energy Storage* **2021**, *39*, 102612.
20. Stark, M.; Krost, G. Neural network based modeling of metal-hydride bed storages for small selfsustaining energy supply systems. In Proceedings of the 2011 IEEE Trondheim PowerTech, Trondheim, Norway, 19–23 June 2011.
21. Bedrunka, M.; Bornemann, N.; Steinebach, G.; Reith, D. Reaction behavior modeling of metal hydride based on FeTiMn using numerical simulations. 2021, *submitted*.
22. Nasrallah, S.; Jemni, A. Heat and mass transfer models in metal-hydrogen reactor. *Int. J. Hydrogen Energy* **1997**, *22*, 67–76. [\[CrossRef\]](#)
23. Steinebach, G.; Dreistadt, D.M. Water and Hydrogen Flow in Networks: Modelling and Numerical Solution by ROW Methods. In *Rosenbrock—Wanner—Type Methods*; Springer: Cham, Switzerland, 2021; pp. 19–47.
24. Steinebach, G.; Dreistadt, D.; Hausmann, P.; Jax, T. Setup of Simulation Model and Calibration. In *Decision Support Systems for Water Supply Systems*; European Mathematical Society Publishing House: Berlin, Germany, 2020; pp. 129–149.
25. Dematteis, E.M.; Dreistadt, D.M.; Capurso, G.; Jepsen, J.; Cuevas, F.; Latroche, M. Fundamental hydrogen storage properties of TiFe-alloy with partial substitution of Fe by Ti and Mn. *J. Alloys Compd.* **2021**, *874*, 159925. [\[CrossRef\]](#)
26. HyCare. Hydrogen CARRIER for Renewable Energy Storage. Available online: <https://hycare-project.eu/> (accessed on 22 December 2021).
27. Fünfgeld, C. Repräsentatives Profil “Haushalt”. 1999. Available online: <https://www.bdew.de/energie/standardlastprofile-strom/> (accessed on 22 December 2021).
28. The MathWorks Inc. Simscape Modellieren und Simulieren von Physikalischen Mehrdomänen Systemen. Available online: <https://de.mathworks.com/products/simscape.html> (accessed on 22 December 2021).

29. The MathWorks Inc. Constant Volume Chamber (G). Available online: <https://de.mathworks.com/help/phymod/simscape/ref/constantvolumechamberg.html> (accessed on 22 December 2021).
30. Feng, F.; Geng, M.; Northwood, D. Mathematical model for the plateau region of P–C-isotherms of hydrogen-absorbing alloys using hydrogen reaction kinetics. *Comput. Mater. Sci.* **2002**, *23*, 291–299. [[CrossRef](#)]
31. Schwarz, R.B.; Khachatryan, A.G. Thermodynamics of open two-phase systems with coherent interfaces. *Phys. Rev. Lett.* **1995**, *74*, 2523–2526. [[CrossRef](#)] [[PubMed](#)]
32. Schwarz, R.; Khachatryan, A. Thermodynamics of open two-phase systems with coherent interfaces: Application to metal–hydrogen systems. *Acta Mater.* **2006**, *54*, 313–323. [[CrossRef](#)]
33. Buchner, H. *Energiespeicherung in Metallhydriden*; Springer: New York, NY, USA, 1982.
34. Herbrig, K.; Röntzsch, L.; Pohlmann, C.; Weißgärber, T.; Kieback, B. Hydrogen storage systems based on hydride–graphite composites: Computer simulation and experimental validation. *Int. J. Hydrogen Energy* **2013**, *38*, 7026–7036. [[CrossRef](#)]
35. Liebig, C.D.D. Systemsimulation und Versuchsdurchführung eines auf PEM Brennstoffzellen Basierten Gas-to-Power-Systems mit Integrierten Metallhydridspeichern. Master’s Thesis, Helmut-Schmidt-Universität Universität der Bundeswehr Hamburg, Hamburg, Germany, 2021.
36. Gnielinski, V. G6 Querumströmte Einzelne Rohre, Drähte und Profilzylinder. In *VDI-Wärmeatlas*; Verein Deutscher Ingenieure: Düsseldorf, Germany, 2013; pp. 817–822.
37. The MathWorks Inc. Pipe (G). Available online: <https://de.mathworks.com/help/phymod/simscape/ref/pipeg.html> (accessed on 22 December 2021).
38. Covarrubias Guarneros, M. Modeling and Parameterization of a PEM Fuel Cell Stack for System Integration into a Metal Hydride Based Hydrogen Storage System. Master’s Thesis, Hamburg University of Applied Sciences, Hamburg, Germany, 2021.
39. Kümmel, W. *Technische Strömungsmechanik: Theorie und Praxis*; Vieweg+Teubner Verlag: Wiesbaden, Germany, 2004.
40. Gambini, M.; Manno, M.; Vellini, M. Numerical analysis and performance assessment of metal hydride-based hydrogen storage systems. *Int. J. Hydrogen Energy* **2008**, *33*, 6178–6187. [[CrossRef](#)]
41. Muthukumar, P.; Maiya, M.P.; Murthy, S.S. Experiments on a metal hydride-based hydrogen storage device. *Int. J. Hydrogen Energy* **2005**, *30*, 1569–1581. [[CrossRef](#)]
42. Capurso, G.; Schiavo, B.; Jepsen, J.; Lozano, G.A.; Metz, O.; Klassen, T.; Dornheim, M. Metal Hydride-Based Hydrogen Storage Tank Coupled with an Urban Concept Fuel Cell Vehicle: Off Board Tests. *Adv. Sustain. Syst.* **2018**, *2*, 1800004. [[CrossRef](#)]